Electronic transport and localization in nitrogen-doped graphene devices using hyperthermal ion implantation

Adam L. Friedman,[1,*] Cory D. Cress,[2] Scott W. Schmucker,[3] Jeremy T. Robinson,[2] and Olaf M. J. van 't Erve[1]

[1]*Materials Science and Technology Division, Naval Research Laboratory, 4555 Overlook Ave., S.W., Washington, DC 20375, USA*

[2]*Electronics Science and Technology Division, Naval Research Laboratory, 4555 Overlook Ave., S.W., Washington, DC 20375, USA*

[3]*National Research Council Postdoctoral Research Associate residing at the U.S. Naval Research Laboratory, Washington, DC 20375, USA*

Hyperthermal ion implantation offers a controllable method of producing high-quality substitutionally doped graphene with nitrogen, an *n*-type dopant that has great potential for graphene electronics and spintronics applications where high carrier concentration, uniform doping, and minimal vacancy defect concentration is desired. Here we examine the transport properties of monolayer graphene sheets as a function of implantation beam energy and dose. We observe a transition from weak to strong localization that varies as a function of carrier concentration. For nominally equivalent doses, increased N ion energy results in an increasing magnetoresistance magnitude, reaching a value of approximately −5.5% at 5000 Oe, which we discuss in the context of dopant concentration and defect formation. We use a model for the temperature dependence of the conductivity that takes into account both temperature activation, due to the formation of a transport gap, and Mott variable-range hopping, due to the formation of defects, to further study the electronic properties of the doped films as a function of dose and N ion energy. We find that the temperature activation component dominates the behavior.

I. INTRODUCTION

Since the discovery that a single atomic layer of sp^2 bonded carbon atoms, termed graphene, could be isolated from bulk graphite in 2004 [1], a plethora of remarkable electronic and spintronic properties have emerged including anomalous magnetoresistance effects, Klein tunneling, anisotropic resistance, and high room temperature spin lifetimes [2–6]. However, few applications are forthcoming because graphene lacks a band gap and its doping is difficult to control [7–9], highly contingent on interactions with the substrate [10,11] and extrinsic impurities [8] rendering graphene devices competitive only for highly specialized device technologies.

Chemical functionalization of graphene facilitates doping and may add a usable transport gap [12–16]. For most published studies, atomic species (e.g., fluorine or hydrogen) are chemically bonded to the surface out-of-plane, breaking the sp^2 symmetry and replacing it an sp^3 bond. These methods produce functionalized graphene, rather than substitutionally doped graphene, where the former is typically only chemically stable for days (e.g., fluorine) or weeks (e.g., hydrogen) or less, depending on environmental conditions [17,18]. Some chemical vapor deposition (CVD) growth methods introduce dopants in the graphene lattice during growth. However, studies indicate that dopants incorporated during growth segregate by sublattice within individual grains and tend to avoid edges and grain boundaries, making doping uniformity difficult to control [19–21]. Functionalization or doping with high-energy ions, such as plasma treatments, produces many vacancy defects in the film, eroding graphene's desirable properties [22,23].

A more recently considered doping method, hyperthermal ion implantation (HyTII), can produce stable [24] substitutionally doped films [25,26]. High-energy irradiated graphene contains many vacancy defects (hereafter simply referred to as "defects"), and was found to result in a transport behavior dominated by hopping conduction due to resonant scattering [27]. In contrast, recent work shows that for a narrow range of hyperthermal ion energies, low-vacancy doping can be realized [28]. For these doped, low defect films, we would expect the transport to be directly correlated to the doping character and not display the hopping-dominated conduction caused by defects.

In another carbon system, diamond, nitrogen is an important dopant for achieving field emission [29], spintronic control [30], and carrier control [31], and is often introduced controllably through ion implantation methods. Moreover, N-doped graphene may have properties that are useful for electronics or spintronics beyond the expected band gap opening, such as a higher carrier concentration [32] or magnetic coupling that results in spin gapless states [33]. A handful of groups have succeeded in creating N-doped graphene. These studies are primarily concerned with material fabrication, chemical, or structural analysis, and, with few exceptions [21,25], performed little to no electronic transport analysis. Furthermore, many of these studies introduced dopants during graphene growth yielding segregated N substituents rather than an even dispersion throughout the film [21]. Doping achieved *via* HyTII provides uniform N coverage [21,28].

In this work, CVD-grown graphene films are substitutionally doped with nitrogen using HyTII in the range of implantation energies where low-vacancy doping is expected. We use a variety of HyTII beam energies and fabricate FET devices exposed to different doses at each beam energy. The magnetoresistance properties of the devices are studied, fitting the behavior to the two-dimensional weak localization model. We observe a crossover from strong to weak localization as a function of carrier concentration and beam dose. We also measure the temperature dependence of the devices, fitting them to a model that considers both Mott variable-range hopping (VRH) and thermal activation (TA).

---

*Corresponding author: adam.friedman@nrl.navy.mil

II. METHODS AND FABRICATION

Graphene is grown by CVD using a low-pressure method on copper foils, described elsewhere [34]. Following growth, we use HyTII to substitutionally dope the graphene directly on the Cu foil growth substrate, which is depicted in the cartoon inset in Fig. 1(a). We implant N^+ ranging in energy from 25 to 65 eV using a Colutron Model G-2-D ion gun with an initial base pressure $<1 \times 10^{-7}$ Torr and an implant pressure of $\sim 3 \times 10^{-6}$ Torr. From the hot-filament ion source, ions are extracted with a 75 eV extraction voltage, accelerated to 600 eV, translated through a Wien filter removing molecular nitrogen ions N_2^+, and finally decelerated to the desired energy with a Colutron Model 400-L Decelerator. We calibrate the beam energy by sweeping the ground potential of a Faraday cup to find the voltage that suppresses the beam current. The full-width at half-maximum of the first derivative (with respect to voltage) of these beam retardation scans provides a measure for the beam energy spread and is <2 eV for all beam energies studied. Following calibration, the beam is expanded to achieve a steady beam current ($\sim 0.1 \mu A/cm^{-2} \times 6.4 \times 10^{11} N^+/cm^2$) within the $0.049\,cm^2$ area of the grounded Faraday cup, and the sample is translated into the stationary beam where it is held until a region on the sample reaches a dose of $5.6 \times 10^{14}\,N^+/cm^2$. Away from the peak dose region, the beam flux gradually subsides over an area with a radius of ~ 1 cm. Within this area, a wide range of beam doses are achieved, each of which are estimated using

Raman spectroscopy as an independent (and internal) dose metric.

Raman spectroscopy (532 nm laser) is used to measure changes in sp^2-carbon bonding as a function of the beam dose for each fabricated device. In Fig. 1(b) the dotted white line in the optical image surrounds the graphene channel, for which we provide a spatial Raman map in the enlarged image depicting the ratio between integrated D peak intensity and the integrated $2D$ peak intensity [the peak intensity ratio $I(D)/I(2D)$ is hereafter abbreviated as $D/2D$], showing the uniformity of the doping over the full surface of the device. The Raman $D/2D$ integrated intensity ratio has been shown to be a sensitive metric of disorder induced in graphene regardless of the origin of the disorder, where vacancies, functionalization, substitutional dopants, and grain boundaries all contribute to an increased $D/2D$ [28]. In contrast, the Raman D/D' integrated intensity ratio is strongly dependent on the type of disorder, and a value near 2 has been associated with quaternary nitrogen substituents [see Fig. 1(a)] in graphene [20,22]. In previous research we used these independent metrics along with STM mapping, density functional theory modeling, and XPS analysis (see Supplemental Material [35]) to identify the N^+ energy range that maximizes the substitutional N doping and minimizes unwanted defect formation to yield doped, low-defect N-graphene [28]. We found this range to be 30–50 eV. For this study we use graphene HyTII-process beam energies of 25, 40, 45, 50, and 65 eV. At 25 eV we expect out-of-plane adatom doping along with substitutional
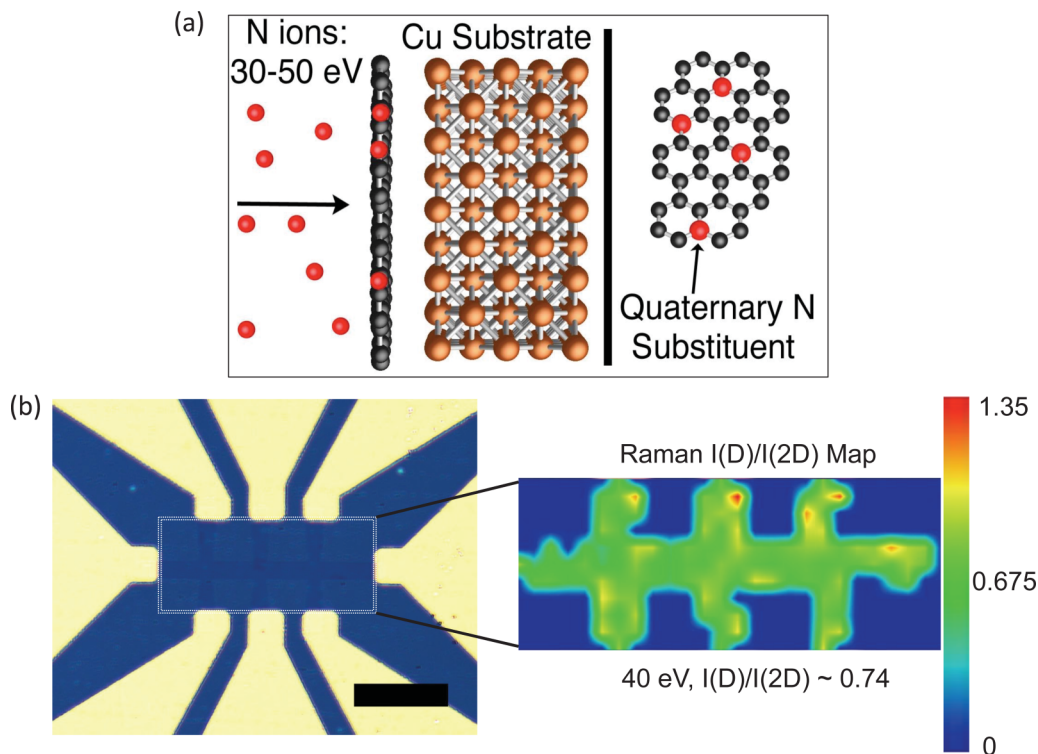

FIG. 1. (a) Cartoon representation of the N-doping process of graphene on Cu foil prior to transfer to SiO_2/Si substrate. N^+ ions in the range of 30–50 eV create N-doped graphene with a low defect density. (b) Optical image of a completed device. The scale bar is 50 μm. The dotted white line surrounds the patterned graphene channel, of which a Raman $I(D)/I(2D)$ map is shown in the blown up section. The Raman map is for a 40 eV device with a $I(D)/I(2D) \sim 0.74$ and shows high uniformity across the entire device. The colors correspond to the ratios as indicated.

doping. Substitutional doping with minimal defect formation occurs for 40, 45, and 50 eV. For 65 eV we expect defect formation along with doping. We also measure devices with different exposure doses (i.e., containing different amounts of N doping), as determined by the Raman $D/2D$ ratio, at each beam energy (discussed further below).

The N-doped graphene films are transferred to 100 nm thermally grown SiO_2/n^+ Si substrate using wet methods described elsewhere [36]. The n^+ Si will later act as the back-gate contact. By doping the films prior to transfer, we avoid scattering caused by ion implantation in the SiO_2/Si [8], which would mask the effects relevant to the present study. Films are patterned into Hall-bar devices using PMMA and deep-UV photolithography, which was found to leave minimal resist residues on the surface of the films [37–39], followed by O_2 plasma etching. A subsequent deep-UV lithography with PMMA step defines trenches for electrical contacts, which are then created by depositing 5 nm/35 nm Ti/Au by electron beam evaporation and liftoff in acetone. An optical image of a completed device is shown in Fig. 1(b).

FET mobilities μ are measured using

$$\mu = \frac{L}{W C_{ox} V_{Drain}} \frac{\partial I}{\partial V_G}\bigg|_{V=constant}. \tag{1}$$

Here L is the channel length (either 50 or 120 μm, depending on which contacts were used), W is the channel width ($= 10$ μm), V_{Drain} is the constant drain voltage, I is the current, V_G is the gate voltage, and $C_{ox} = 3.45 \times 10^{-4}$ F/m^2, the capacitance of the oxide. Witness devices made from undoped CVD graphene had mobilities in the range of 3000–5000 cm^2/Vs at 10 K near the Dirac point. Devices doped at all beam energies had $\mu \sim$ 200–1000 cm^2/Vs at 10 K near the Dirac point. The significant decrease in mobility for implanted devices is expected and is evidence of successful band structure modification. However, a decrease in mobility is expected for both doped and defect disordered devices, so

it cannot serve as a reliable comparison metric between these low defect films and previously studied high defect films [27]. For devices that received a very high dose, mobilities were lower than 100 cm^2/Vs. All devices had hole mobilities that were slightly higher than electron mobilities, regardless of doping beam energy or dose. This asymmetry is a phenomenon observed in other transport studies of CVD graphene [8], and is related to the transport properties of the graphene-metal contact interface [40].

Electrical measurements are taken in a variable temperature cryo-free cryostat and electromagnet setup. We employ four-terminal electrical measurements of the longitudinal resistance or conductance, which eliminates contributions from the contacts.

III. RESULTS AND ANALYSIS

A. Raman characterization of dose

In Fig. 2(a) we plot the spatially averaged Raman spectra for nine graphene Hall bar structures N-HyTII processed with 40 eV N$^+$ ions as an example of the Raman analysis that was performed for all beam energies used in this study. The spectra are normalized to their G-peak intensity and arranged in order of their $D/2D$ ratio (from top to bottom). The evolution of the Raman spectrum from the nearly pristine (top) graphene to highly doped includes a substantial increase in the D peak ($\sim$1343 cm^{-1}) and D' peak ($\sim$1624 cm^{-1}) intensities, with a corresponding decrease in $2D$ peak ($\sim$2681 cm^{-1}) intensity. Additionally, all peaks broaden with doping. In all spectra, the D/D' integrated intensity ratio is between 1.8 and 2.2 consistent with N substitutional doping. In Fig. 2(b) we plot the Raman G-peak frequency, for the same series of samples, as a function of the integrated $D/2D$ ratio. As the $D/2D$ increases, we observe a blue shift in the G peak frequency of over 5cm^{-1}, which corresponds with an estimated electron doping of over 4×10^{12} cm^{-2} [41]. G-peak shifts are not
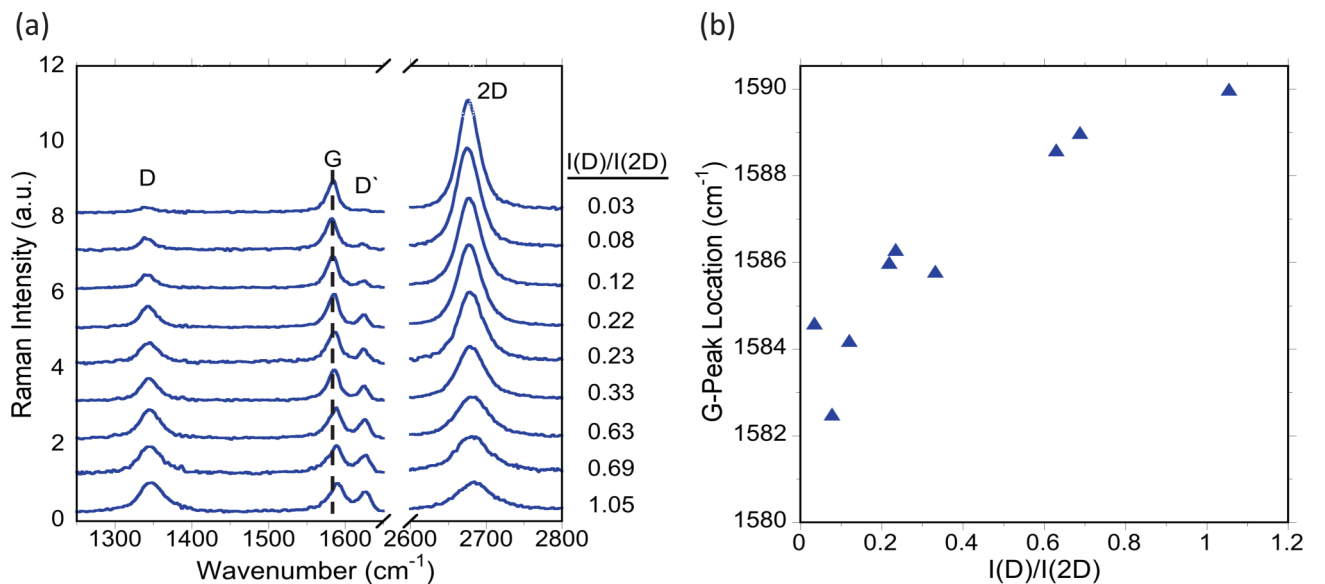

FIG. 2. (a) Spatially averaged Raman spectra for devices implanted with 40 eV N$^+$ ions normalized to the G-peak intensity and arranged according to $I(D)/I(2D)$ ratio (equated to dose). The dotted black line is a guide for the eye to better visualize the shifting G peak as a function of implantation dose. (b) Raman G-peak frequency vs $I(D)/I(2D)$ ratio.
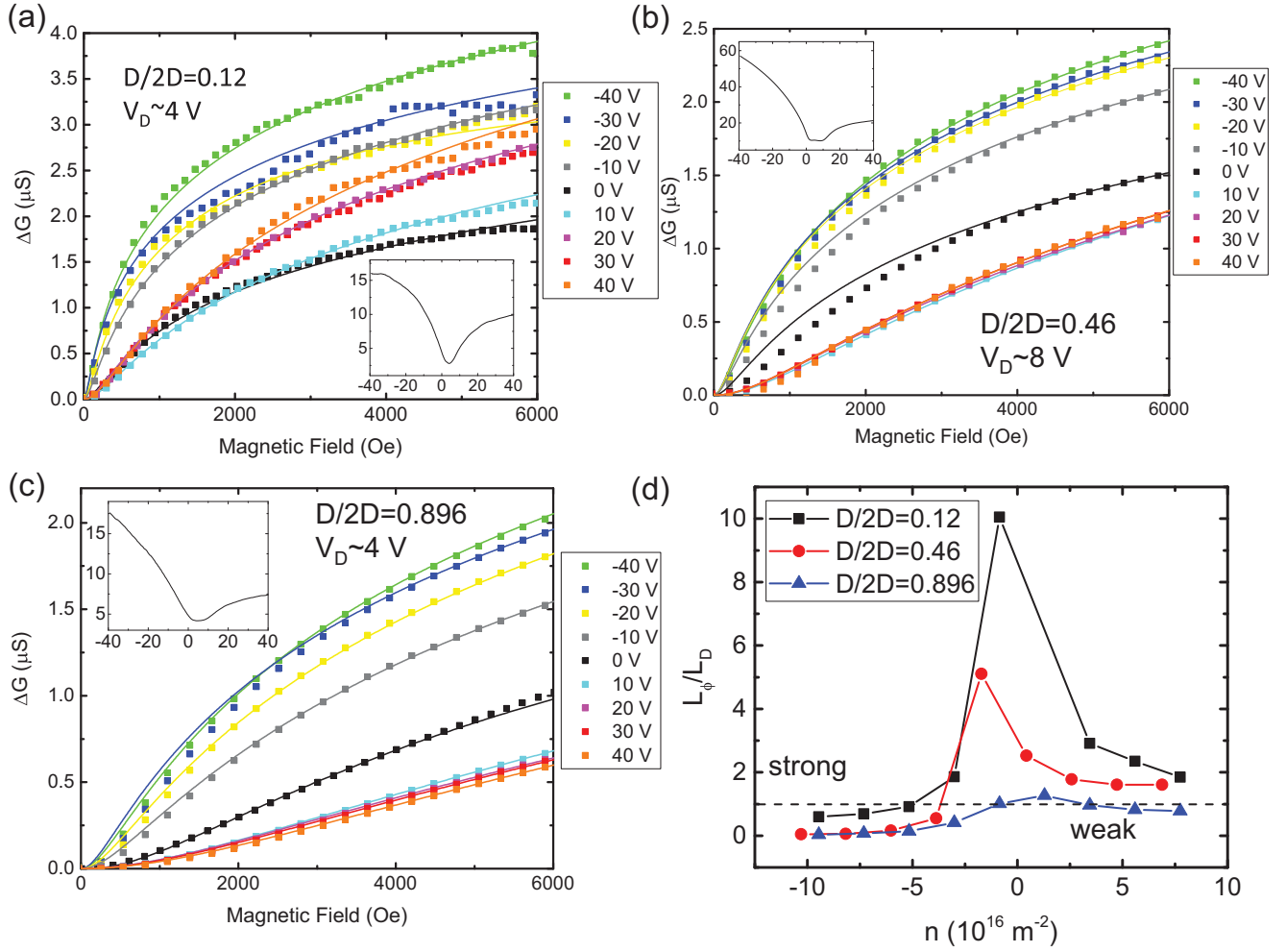
FIG. 3. (a)–(c) Conductance vs magnetic field at a variety of back-gate voltages for devices with $D/2D$ ratios of 0.12, 0.46, and 0.896, respectively. The dotted lines show the data and the solid lines show the fits to the $2D$ weak localization model. The insets show the conductance (y axis: μS) vs back-gate voltage (x axis: V). HyTII beam energy for these devices was 45 eV. (d) Ratio of fitting parameters extracted from the fits in (a)–(c) vs carrier concentration for the three $D/2D$ ratios. Above the dotted line is strong localization and below the dotted line is weak localization.

observed for vacancy-only formation in the range of $D/2D$ values explored, and are a direct result of doping [27]. Further evidence of doping in these films can be found in Ref. [28].

B. Magnetoconductance and localization

Figures 3(a)–3(c) show the change in magnetoconductance with respect to zero field as a function of magnetic field for a sample exposed to a beam energy of 45 eV for three different doses ($D/2D$ of 0.12, 0.46, and 0.896, respectively) and a variety of back-gate voltages (e.g., carrier concentrations). Measured data are shown as points in these plots. The insets show the conductance in μS vs back-gate voltage for the devices, and the position of the Dirac point (V_D) is indicated. The broad, double conductance minimums seen for the higher dosed samples are a possible indication of low-energy resonant scattering [42] from increased substitutional nitrogen, which has been observed previously in other types of doped graphene devices [43]. For undoped devices, Dirac points are generally higher than 15 V. For doped devices, the Dirac points are closer to $n = 0$, which is expected due to the strong n-doping

properties of nitrogen. For the experiment in Fig. 3, a 45 eV implantation energy was chosen based on a previous study that determined that this beam energy is in the range where doping is maximized and defects are minimized [28].

Localization is a major contributor to the magnetoresistance in doped, disordered, and functionalized graphene films at low temperature. Here broken chiral symmetry leads to intervalley scattering and electronic self-intersecting scattering paths resulting in constructive quantum interference, the amount of which decreases with increasing magnetic field. This manifests as a decrease in resistivity. Detailed theoretical analysis and further explanation can be found in the literature [44–50]. The two-dimensional localization model is used to fit and analyze the data [46–48]:

$$\Delta G = G - G(0) = \frac{Ae^2}{\pi h}\left[F\left(\frac{\tau_B^{-1}}{\tau_\varphi^{-1}}\right) - F\left(\frac{\tau_B^{-1}}{\tau_\varphi^{-1} - 2\tau_{\text{inter}}^{-1}}\right)\right.$$
$$\left. - 2F\left(\frac{\tau_B^{-1}}{\tau_\varphi^{-1} + \tau_{\text{inter}}^{-1} + \tau_{\text{intra}}^{-1}}\right)\right]. \quad (2)$$

Here G is the conductance and A is a proportionality constant that also contains information about the device dimensions. $F(x) = \ln(x) + \psi(0.5 + x^{-1})$, with $\psi(x)$ being the digamma function. $\tau^{-1}_{\text{inter,intra}}$, the intervalley scattering time due to weak point disorder and the intravalley scattering time due to charged-impurity disorder, respectively, are calculated by

$$\tau^{-1}_{\text{inter}} = \frac{\sigma_{\text{SR}}h}{2e^2 v_F (\pi n)^{1/2}}, \tag{3a}$$

$$\tau^{-1}_{\text{intra}} = \frac{h\mu n^{1/2}}{2e v_F \pi^{1/2}}. \tag{3b}$$

The conductivity due to short-range disorder σ_{SR} is calculated using $\sigma^{-1} = \sigma_{\text{SR}}^{-1} + \sigma_D^{-1}$, where it is assumed that localization effects are negligible at higher temperatures (see Supplemental Material for examples of room-temperature field-sweep data [35]). $\sigma_D = en\mu$, the Drude conductivity measured at 100 K, and σ is the measured low-temperature conductivity. The carrier concentration n is calculated using $n = \alpha(V_g - V_D)$. V_g is the applied back-gate voltage, V_D is the measured Dirac, or charge neutrality point, and $\alpha = \varepsilon_r \varepsilon_0 / te$, the areal capacitance calculated using a parallel plate capacitor model. ε_r is the dielectric constant of SiO_2, ε_0 is the permittivity of free space, t is the back-gate oxide thickness ($= 100$ nm), e is the elementary charge of an electron, v_F is the Fermi velocity ($\sim 10^6$ m/s for graphene), and h is Planck's constant. $\tau^{-1}_B = 4eDB/h$, with the diffusion constant $D = 0.5 v_F (\tau^{-1}_{\text{inter}} + \tau^{-1}_{\text{intra}})$ and $B =$ magnetic field. The phase relaxation time $\tau^{-1}_\varphi = L^2_\varphi / D$, which is a measure of how long the electron maintains its phase coherence, is the fitting parameter for the model. The solid lines in Figs. 3(a)–3(c) are the best-fit lines to the data using Eq. (2). The data are in good agreement with the model.

Localization type for the devices is determined by comparing the fit-extracted phase relaxation length L_φ (length over which the electron maintains its phase coherence) with the localization length $L_D = L_e \exp(\sigma_D h / e^2)$. Here $L_e = \sigma_D h / 2e^2 (\pi n)^{1/2}$, the electron localization, or elastic scattering length. When $L_\varphi > (<) L_D$, there is strong (weak) localization. The transition from the electron scattering and phase coherence effects described by weak localization and the metal-insulator type transition described by strong or Anderson localization remains a subject of much interest in a variety of graphene treated graphene films, as the type of localization sheds light on the scattering processes created by the dopants and helps elucidate band structure changes [43,46–49]. Figure 3(d) summarizes the localization character as a function of dose and carrier concentration for the 45 eV N-HyTII processed samples in terms of the ratio L_φ / L_D. A dotted line at $L_\varphi / L_D = 1$ denotes the transition between strong (>1) and weak (<1) localization. Note that an undoped witness device displayed weak localization near the Dirac point with $L_\varphi / L_D \sim 1 \times 10^{-10}$, indicating an extremely long electron localization length and a comparatively much shorter phase relaxation length (see Supplemental Material for more information [35]). This is in stark contrast to the doped samples, which all displayed strong localization near their respective Dirac points. Moreover, there is a carrier concentration-induced transition from weak to strong localization for all of the doped samples.
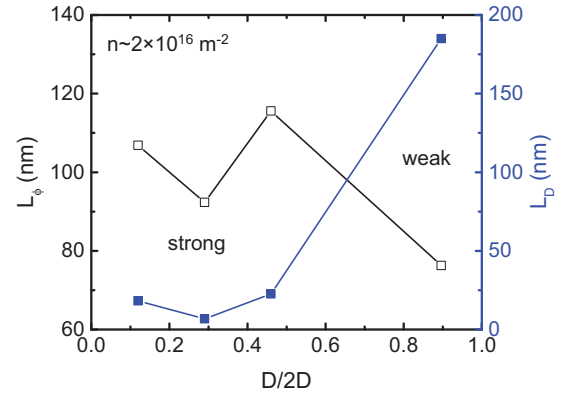

FIG. 4. Phase relaxation length and localization length vs $D/2D$ ratio. Carrier concentration (holes, in this case) is $\sim 2 \times 10^{16}$ for each data point. HyTII beam energy is 45 eV. The black open squares are for L_φ and go with the left axis, and the blue closed squares are for L_D and go with the right axis. The crossing of the two lines indicates a transition from strong to weak localization as the $D/2D$ ratio increases.

However, the magnitude of the characteristic lengths ratio, or "strength" of the strong localization decreases steadily as the dose increases. L_φ / L_D roughly follows the shape of the gate sweep curves, with the higher mobility hole side being weakly localized, while the lower mobility electron side is strongly localized. However, the highest dosed sample $D/2D = 0.896$ only remains strongly localized for a narrow range of carrier densities around the Dirac point before it returns to a weakly localized state. This is intriguing, as it indicates that a higher amount of nitrogen doping prevents the crossover to insulating behavior near the Dirac point.

Figure 4 shows the characteristic lengths extracted from fits to the $2D$ weak localization model vs implantation dose for a constant carrier concentration (holes) of $\sim 2 \times 10^{16}$ m^{-2}. Where the L_φ line (in black, open squares) crosses the L_D line (in blue, closed squares) indicates a transition from strong to weak localization. Devices are weakly localized for no nitrogen doping near the Dirac point (see Supplemental Materials [35]). The doped devices are strongly localized for low doses and then transition back to weak localization for higher doses. Undoped devices have a very long L_D, or localization lengths, as there are few sources of scattering. The phase relaxation lengths are on order of 100 nm. When the devices are doped, L_D decreases precipitously, while the phase relaxation lengths remain mostly unchanged. However, increasing the dose past where the Raman $D/2D \sim 0.5$ results in L_D increasing again while the phase relaxation length decreases very slowly.

L_φ is more affected by charged impurities and defects and L_D is more affected by scattering that would cause changes in the conductivity [46,47,49]. The slow decrease in the phase relaxation length as a function of dose is therefore understood as an increase in substitutional nitrogen content. The initial large decrease in L_D for doped as compared to undoped devices is also understood as likely a combination of an increase in impurity density, scattering caused by nitrogen,
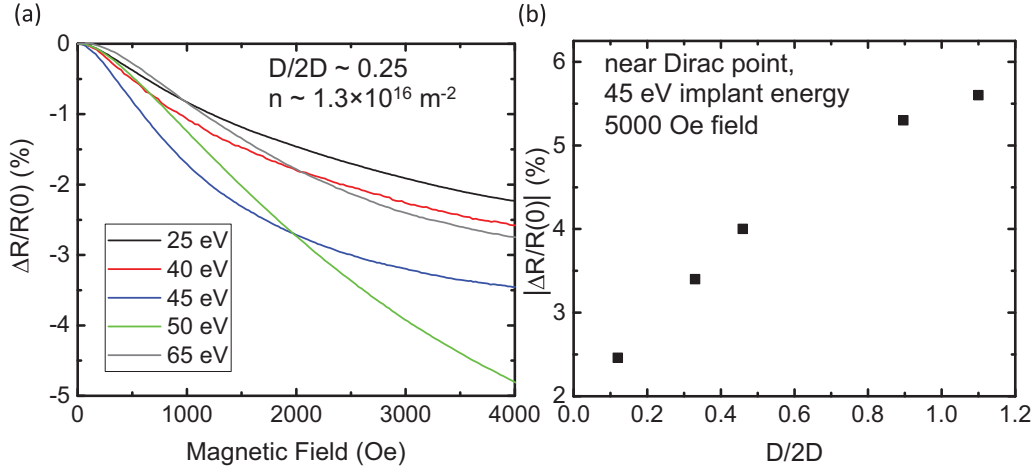
FIG. 5. (a) Magnetoresistance as a function of HyTII beam energy for $D/2D$ ratio of ∼0.25 at a carrier concentration (holes) of ∼1.3×10^{16}. (b) Magnitude of magnetoresistance vs $D/2D$ ratio near the Dirac point and at 5000 Oe. HyTII beam energy was 45 eV.

and possibly the opening of a band gap. However, at this time, we are unable to explain why L_D begins to increase again for larger doses, as it seems counterintuitive. Indeed, a sample prepared with a beam energy of 50 eV and a $D/2D = 4.79$, representing a very large dose, gives an L_D of 0.1 nm and L_φ of 30 nm, consistent with expectations.

C. Magnetoresistance

Figure 5(a) shows the magnetoresistance MR = $[R(B_{\text{perpendicular}}) - R(0)]/R(0) \times 100$ as a function of beam energy for a constant $D/2D$∼0.25 and $n \sim 1.3 \times 10^{16}\,\text{m}^{-2}$ (holes). As the incident ion energy increases, so does the magnitude of the large negative MR, with exception of the highest beam energy (65 eV). The large negative MR is likely due to successful nitrogen incorporation, as dilute graphene dopants, for example fluorine [49] and hydrogen [46], have also resulted in a large negative MR, while small amounts of disorder and defects leads to large positive MR [4]. Adatom- and doping-induced large negative MR is thought to arise either from either (i) broken time-reversal symmetry and suppression of quantum interference [50], (ii) magnetic polaron formation originating in delocalized electron spins [51] caused by the dopants, or (iii) a combination of these two mechanisms [49]. For higher beam energies (for instance, 65 eV), a lower doping efficiency is predicted by molecular dynamics, resulting from a lower probability of nitrogen substitution and a larger probability of defect (e.g., vacancies) formation [52]. As the beam energy increases in the range of 30–50 eV (where few defects are expected), more dopants are added. Therefore, an increase in the magnitude of MR with beam energies up to 50 eV, followed by a change in the MR characteristics at 65 eV, is expected and consistent with our experimental findings.

Figure 5(b) shows the magnitude of the MR as a function of dose for a beam energy of 45 eV and applied magnetic field of 5000 Oe. As the dose increases, so does the magnitude of the MR, until it begins to saturate asymptotically at higher doses. An MR as large as ∼ −5.5% is observed at 5000 Oe for films with a $D/2D$ of ∼ 1.1. The saturation of the MR magnitude

is entirely consistent with the understanding of the origins of the large MR effect offered above.

D. Temperature dependence of the conductivity

Studies of other doped graphene devices have relied on either the Mott variable-range hopping model (VRH) or a thermal activation model (TA) to describe the temperature dependence of their devices. The VRH model is given by $\sigma = A\exp[-(T/T_0)^{1/3}]$. The TA model is given by $\sigma = B\exp[-E_g/2k_BT]$. However, we found that neither model fits our data adequately. Previous experiments of disordered or functionalized graphene devices have reported a disorder-dependent crossover between VRH and TA behavior [44,47]. We found no conditions for which either model was a good fit to the data alone. In other studies, disorder and the presence of localized states have been shown to lead to temperature dependence that behaves like VRH at higher temperatures and TA at lower temperatures. Mainly, for instance, in bilayer graphene devices in a large perpendicular electric field, it was found that a better model is a sum of both models, such that [53]

$$\sigma = \text{VRH} + \text{TA} = A\exp\left[-\left(\frac{T_0}{T}\right)^{1/3}\right] + B\exp\left[-\frac{E_g}{2k_BT}\right]. \tag{4}$$

Here A and B are proportionality constants, T is temperature, k_B is Boltzmann's constant, E_g is the transport gap, and T_0 is the characteristic temperature. T_0 is related to the density of localized states at the Fermi energy $N(E_F)$ by [49,54]

$$T_0 = \frac{13.8}{k_B N(E_F) L_D^2}. \tag{5}$$

The comparative magnitudes of E_g and $k_B T_0$ (both in units of eV) reveal the strength of each of the respective components of the model. We expect that the hopping conduction component will be small compared to the band component for our devices that have substitutional nitrogen and minimal defects, contrary to previous studies where defects dominate [27,47].

Figure 6(a) shows conductivity vs $1000/T$ for a sample processed with a 40 eV beam energy and a $D/2D$ ratio of
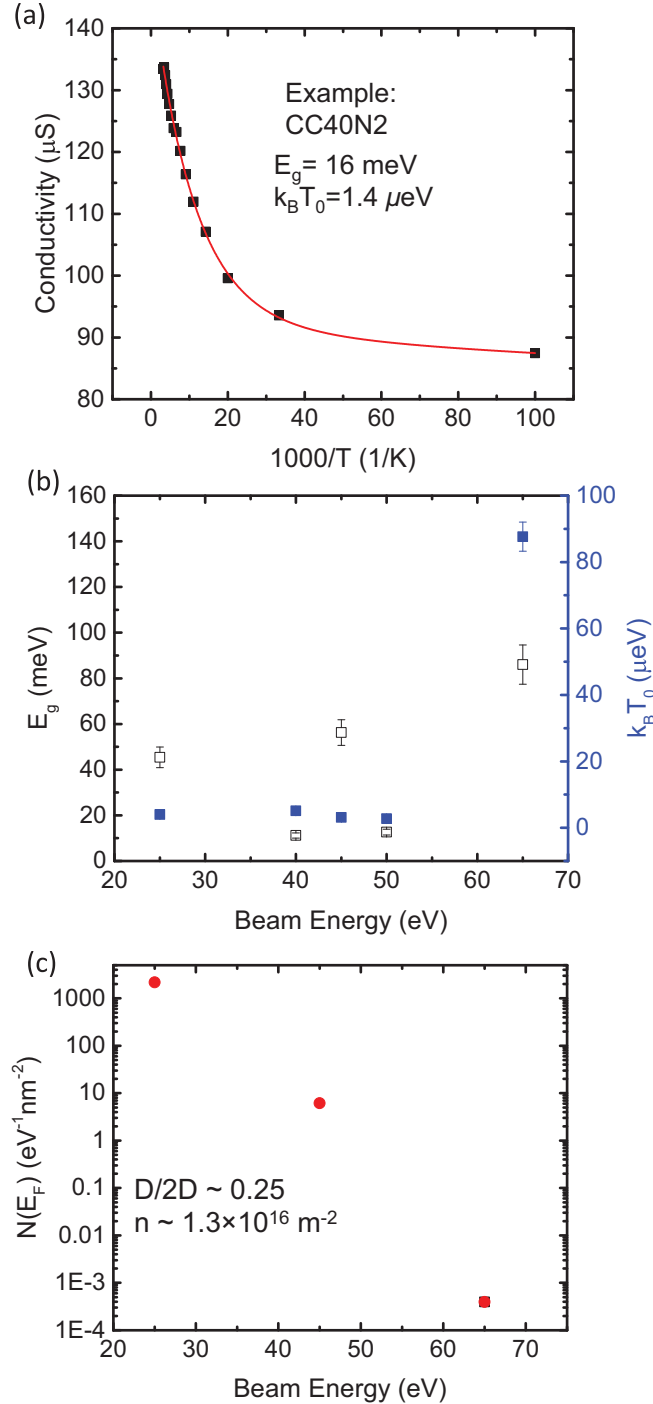
FIG. 6. (a) Conductivity vs $1000/T$ (black points) and fits to the VRH + TA model near the Dirac point for device CC40N2, which is used as an example showing the typical goodness of fit. The implantation energy was 40 eV and the dose was $D/2D \sim 0.85$. The fitting parameters are as indicated. (b) VRH + TA fitting parameters vs HyTII beam energy for $D/2D \sim 0.25$ near the Dirac point. The black open squares are for E_g and go with the left axis, and blue closed squares are for $k_B T_0$ and go with the right axis. (c) Density of states at the Fermi energy vs beam energy for a carrier concentration of $\sim 1.3 \times 10^{16}$ m^{-2} and $D/2D \sim 0.25$.

0.85. The data are the black points, and the fit to Eq. (4) is the red line. The data fit the model well. From the fit we extract

$E_g \sim 16$ meV and $k_B T_0 \sim 1.4$ μeV. The fact that the VRH + TA model fits our data, rather than observing a crossover between each model as a function of doping or hoping-dominated conduction alone, indicates the difference between previous functionalized adatom type doping or high-energy high defect resultant irradiated films and the substitutional doping methods employed here. The size of the extracted transport gap is similar to that found in other studies of doped graphene [14,15,53].

Figure 6(b) shows a plot of E_g and $k_B T_0$ vs beam energy. The transport gap remains fairly consistent for all beam energies except 65 eV, which is expected since all energies here result in nominally equivalent substitutionally doped graphene. Likewise, $k_B T_0$ remains mostly constant, but increases suddenly for the 65 eV beam energy. These results indicate that the 65 eV N-HyTII processed samples do indeed possess a higher defect concentration. Comparing the size of the fitting parameters, the behavior is mostly of the thermal activation type, as expected. We find $k_B T_0$ values in the μeV range and transport gap values in the meV range for all devices tested. Although these E_g values are consistent with other studies of doped graphene films, the values of $k_B T_0$ are significantly lower [14,15,47,53], which, again, is a good indicator of doping rather than defects. Contrary to expectations, we observed no direct correlation between the fitting parameters of Eq. (4) and $D/2D$ ratio, or dose (see Supplemental Material [35]). However, this could simply indicate that the doses of the devices tested (mostly between $D/2D$ of 0.1 and 1) were not high enough to observe any effect.

Using Eq. (5) and the value of the localization length calculated previously, we can extract the density of states at the Fermi energy. Figure 6(c) shows $N(E_F)$ for samples processed with a $D/2D \sim 0.25$ for beam energies 25, 45, and 65 eV at a carrier (hole) concentration $n \sim 1.3 \times 10^{16}$ m^{-2}. A trend is observed in that for higher beam energies, the density of states decreases exponentially. The three devices represent the range of doping behaviors available for N HyTII implanted graphene: 25 eV has substitutionally doped nitrogen and some adatom formation, 45 eV has substitutionally doped nitrogen and low defects, and 65 eV has some substitutionally doped nitrogen and many defects. As the presence of dilute nitrogen incorporated into the carbon lattice is expected to result in an enhanced density of states and greater carrier concentration [55], we suspect that the observed decrease is mostly due to defects at 65 eV. This makes sense, as higher beam energies can cause higher defect densities, lowering the overall conductive properties of the films. Interestingly, no direct correlation between $N(E_F)$ and $D/2D$ was observed inside the range of the $D/2D$ values tested. For most devices, $N(E_F)$ ranged from 1 to 300 eV^{-1} nm^{-2}. As most of the devices, regardless of $D/2D$ ratios measured, had similar conductivities and mobilities, we suspect that for the doses that we used in this study, not enough nitrogen was implanted or enough defects created to observe a change in $N(E_F)$.

IV. CONCLUSION

In conclusion, we have used HyTII to substitutionally dope graphene films with nitrogen. Devices made from these films

show a transition from strong to weak localization that strongly depends on implantation dose, indicating the implanted nitrogen's ability to alter the intrinsic properties of the film. The observed large negative MR, as high as $\sim -5.5\%$ at 5000 Oe, is typical of doped graphene devices, and can be attributed to possible quantum effects or interactions with delocalized moments. As further evidence of the high electronic quality of the implanted devices over similar adatom-doped devices, the temperature dependence can be fit by a model that takes into account both band effects due to the substitutional doping and insulatorlike effects due to defect formation, with the band effects observed to be the major component. Defects only appear to dominate the behavior at large implantation energies, further demonstrating the differences between true-doped films and previous defective/doped films. Therefore, HyTII graphene films have great potential for applications for high-quality graphene where a transport or band gap is desired.

[1] K. S. Novoselov, A. K. Geim, S. V. Morozov, D. Jiang, Y. Zhang, S. V. Dubonos, I. Grigorieva, and A. A. Frisov, Electric field effect in atomically thin carbon films, Science **306**, 666 (2004).

[2] K. S. Novoselov, V. I. Fal'ko, L. Colombo, P. R. Gellert, M. G. Schwab, and K. Kim, A roadmap for graphene, Nature (London) **490**, 192 (2012).

[3] N. Tombros, C. Jozsa, M. Popinciuc, H. T. Jonkman, and B. J. van Wees, Electronic spin transport and spin precession in single graphene layers at room temperature, Nature (London) **448**, 571 (2007).

[4] A. L. Friedman, J. L. Tedesco, P. M. Campbell, J. C. Culbertson, E. Aifer, F. K. Perkins, R. L. Myers-Ward, J. K. Hite, C. R. Eddy, Jr., G. G. Jernigan, and D. K. Gaskill, Quantum linear magnetoresistance in multilayer epitaxial graphene, Nano Lett. **10**, 3962 (2010).

[5] O. M. J. van 't Erve, A. L. Friedman, E. Cobas, C. H. Li, J. T. Robinson, and B. T. Jonker, Low-resistance spin injection into silicon using graphene tunnel barriers, Nat. Nanotech. **7**, 737 (2012).

[6] A. F. Young, and P. Kim, Quantum interference and Klein tunneling in graphene heterojunctions, Nat. Phys. **5**, 222 (2009).

[7] C. Caillier, D.-K. Ki, Y. Lisunova, I. Gaponenko, P. Paruch, and A. F. Morpurgo, Identification of a strong contamination source for graphene in vacuum systems, Nanotechnology **24**, 405201 (2013).

[8] C. D. Cress, J. G. Champlain, E. S. Esqueda, J. T. Robinson, A. L. Friedman, and J. J. McMorrow, Total ionizing dose induced charge carrier scattering in graphene devices, IEEE Trans. Nucl. Sci. **59**, 3045 (2012).

[9] J.-H. Chen, C. Jang, S. Adam, M. S. Fuhrer, E. D. Williams, and M. Ishigami, Charged-impurity scattering in graphene, Nat. Phys. **4**, 377 (2008).

[10] S. Y. Zhou, G.-H. Gweon, A. V. Fedorov, P. N. First, W. A. de Heer, D.-H. Lee, F. Guinea, A. H. Castro Neto, and A. Lanzara, Substrate-induced bandgap opening in epitaxial graphene, Nat. Mater. **6**, 916 (2007).

[11] A. V. Kretinin, Y. Cao, J. S. Tu, G. L. Yu, R. Jalil, K. S. Novoselov, S. J. Haigh, A. Gholinia, A. Mishchenko, M. Lozada, T. Georgiou, C. R. Woods, F. Withers, P. Blake, G. Eda, A. Wirsig, C. Hucho, K. Watanabe, T. Taniguchi, A. K. Geim, and R. V. Gorbachev, Electronic properties of graphene encapsulated with different two-dimensional atomic crystals, Nano Lett. **14**, 3270 (2014).

[12] D. C. Elias, R. R. Nair, T. M. G. Mohiuddin, S. V. Morozov, P. Blake, M. P. Halsall, A. C. Ferrari, D. W. Boukhvalov, M. I. Katsnelson, A. K. Geim, and K. S. Novoselov, Control of graphene's properties by reversible hydrogenation: Evidence for graphene, Science **323**, 610 (2009).

[13] J. T. Robinson, J. S. Burgess, C. E. Junkermeier, S. C. Badescu, T. L. Reinecke, F. K. Perkins, M. K. Zalalutdniov, J. W. Baldwin, J. C. Culbertson, P. E. Sheehan, and E. S. Snow, Properties of fluorinated graphene films, Nano Lett. **10**, 3001 (2010).

[14] B. R. Matis, J. S. Burgess, F. A. Bulat, A. L. Friedman, B. H. Houston, and J. W. Baldwin, Surface doping and band gap tunability in hydrogenated graphene, ACS Nano **6**, 17 (2012).

[15] H. Gao, L. Wang, J. Zhao, F. Ding, and J. Lu, Band gap tuning of hydrogenated graphene: H coverage and configuration dependence, J. Phys. Chem. C **115**, 3236 (2011).

[16] Z. Luo, T. Yu, K.-J. Kim, Z. Ni, Y. You, S. Lim, Z. Shen, S. Want, and J. Lin, Thickness-dependent reversible hydrogenation of graphene layers, ACS Nano **3**, 1781 (2009).

[17] R. Stine, W.-K. Lee, K. E. Whitener, Jr., J. T. Robinson, and P. E. Sheehan, Chemical stability of graphene fluoride produced by exposure to XeF_2, Nano Lett. **13**, 4311 (2013).

[18] K. E. Whitener, Jr., W. K. Lee, P. M. Campbell, J. T. Robinson, and P. E. Sheehan, Chemical hydrogenation of single-layer graphene enables completely reversible removal of electrical conductivity, Carbon **72**, 348 (2014).

[19] L. Zhao, M. Levendorf, S. Goncher, T. Schiros, L. Palova, A. Zabet-Khosousi, K. T. Rim, C. Gutierrez, D. Nordlund, C. Jaye, M. Hybertsen, D. Reichman, G. W. Flynn, J. Park, and A. N. Pasupathy, Local atomic and electronic structure of boron chemical doping in monolayer graphene, Nano Lett. **13**, 4659 (2013).

[20] L. Zhao, R. He, A. Zabet-Khosousi, K. S. Kim, T. Schiros, M. Roth, P. Kim, G. W. Flynn, A. Pinczuk, and A. N. Pasupathy, Dopant segregation in polycrystalline monolayer graphene, Nano Lett. **15**, 1428 (2015).

[21] A. Zabet-Khosousi, L. Zhao, L. Pavlova, M. S. Hybertsen, D. R. Reichman, A. N. Pasupathy, and G. W. Flynn, Segregation of sublattice domains in nitrogen doped graphene, J. Am. Chem. Soc. **136**, 1391 (2014).

[22] A. Eckmann, A. Felten, A. Mishchenko, L. Britnell, R. Krupke, K. S. Novoselov, and C. Casiraghi, Probing the nature of defects in graphene by Raman spectroscopy, Nano Lett. **12**, 3925 (2012).

[23] N. M. R. Peres, F. Guinea, and A. H. Castro Neto, Electronic properties of disordered two-dimensional carbon, Phys. Rev. B **73**, 125411 (2006).

[24] J. H. Warner, Y. C. Lin, K. He, M. Koshino, and K. Suenaga, Stability and spectroscopy of single nitrogen dopants in graphene at elevated temperatures, ACS Nano **8**, 11806 (2014).

[25] P. Wilke, J. A. Amani, A. Sinterhauf, S. Thakur, T. Kotzott, T. Druga, S. Weikert, K. Maiti, H. Hofsass, and M. Wenderoth, Doping of graphene by low-energy ion beam implantation: Structural, electronic, and transport properties, Nano Lett. **15**, 5110 (2015).

[26] U. Bangert, W. Pierce, D. M. Kepaptsoglou, Q. Ramasse, R. Zan, M. H. Gass, J. A. Van den Berg, C. B. Boothroyd, J. Amani, and H. Hofsass, Ion implantation—Toward IC compatible technologies, Nano Lett. **13**, 4902 (2013).

[27] G. Buchowicz, P. R. Stone, J. T. Robinson, C. D. Cress, J. W. Beeman, and O. D. Dubon, Correlation between structure and electrical transport in ion-irradiated graphene grown on Cu foils, Appl. Phys. Lett. **98**, 032102 (2011).

[28] C. D. Cress, S. W. Schmucker, A. L. Friedman, P. Dev, J. C. Culbertson, J. W. Lyding, and J. T. Robinson, Nitrogen-doped graphene and twisted bilayer graphene via hyperthermal ion implantation with depth control, ACS Nano **10**, 3714 (2016).

[29] R. Kalish, C. Uzan-Saguy, B. Philosoph, V. Richter, J. P. Lagrange, E. Gheeraert, A. Deneuville, and A. T. Collins, Nitrogen doping of diamond by ion implantation, Diamond Related Mater. **6**, 516 (1997).

[30] S. D. Bader and S. S. P. Parkin, Spintronics, Annu. Rev. Condens. Matter Phys. **1**, 71 (2010).

[31] C. D. Weis, A. Schuh, A. Batra, A. Persaud, I. W. Rangelow, J. Bokor, C. C. Lo, S. Cabrini, E. Sideras-Haddad, G. D. Fuchs, R. Hanson, D. D. Awschalom, and T. Schenkel, Single atom doping for quantum device development in diamond and silicon, J. Vac. Sci. Technol. B **26**, 2596 (2008).

[32] L. Zhao, R. He, K. T. Rim, T. Schiros, K. S. Kim, H. Zhous, C. Gutierrez, S. P. Chockalingam, C. J. Arguello, L. Pavlova, D. Nordlund, M. S. Hybertsen, D. R. Reichman, T. F. Heinz, P. Kim, A. Pinczuk, G. W. Flynn, and A. N. Pasupathy, Visualizing individual nitrogen dopants in monolayer graphene, Science **333**, 999 (2011).

[33] Y. Li, Z. Zhou, P. Shen, and Z. Chen, Spin gapless semiconductor-metal-half-metal properties in nitrogen-doped zigzag graphene nanoribbons, ACS Nano **3**, 1952 (2009).

[34] X. Li, C. W. Magnuson, A. Venugopal, R. M. Tromp, J. B. Hannon, E. M. Vogel, L. Colombo, and R. S. Ruoff, Large-area graphene single crystals grown by low-pressure chemical vapor deposition of methane on copper, J. Am. Chem. Soc. **133**, 2816 (2011).

[35] See Supplemental Material at http://link.aps.org/supplemental/10.1103/PhysRevB.93.161409 for XPS data taken on the implanted films, room temperature magnetic field dependent magnetoresistance data, fitted magnetoresistance and temperature dependent resistance data taken on an unimplanted witness sample, characteristic lengths vs beam energy data, and temperature dependence model fit parameters vs implantation dose data.

[36] J. T. Robinson, S. W. Schmucker, C. B. Diaconescu, J. P. Long, J. C. Culbertson, T. Ohta, A. L. Friedman, and T. E. Beechem, Electronic hybridization of large-area stacked graphene films, ACS Nano **7**, 637 (2013).

[37] E. Cobas, A. L. Friedman, O. M. J. van 't Erve, J. T. Robinson, and B. T. Jonker, Graphene as a tunnel barrier: Graphene base magnetic tunnel junctions, Nano. Lett. **12**, 3000 (2012).

[38] A. L. Friedman, O. M. J. van 't Erve, J. T. Robinson, K. E. Whitener, Jr., and B. T. Jonker, Hydrogenated graphene as a homoepitaxial tunnel barrier for spin and charge transport in graphene, ACS Nano **9**, 6747 (2015).

[39] H. N. Arnold, V. K. Sangwan, S. W. Schmucker, C. D. Cress, K. A. Luck, J. T. Robinson, T. J. Marks, A. L. Friedman, and M. C. Hersam, Reducing flicker noise in graphene grown by chemical vapor deposition, Appl. Phys. Lett. **108**, 073108 (2016).

[40] B. Huard, N. Stander, J. A. Sulpizio, and D. Goldhaber-Gordon, Evidence of the role of contacts on the observed electron-hole asymmetry in graphene, Phys. Rev. B **78**, 121402(R) (2008).

[41] J. Yan, Y. Zhang, P. Kim, and A. Pinczuk, Electric Field Effect Tuning of Electron-Phonon Coupling in Graphene, Phys. Rev. Lett. **98**, 166802 (2007).

[42] D. M. Basko, Resonant low-energy electron scattering on short-range impurities in graphene, Phys. Rev. B **78**, 115432 (2008).

[43] B. R. Matis, B. H. Houston, and J. W. Baldwin, Low-energy resonant scattering from hydrogen impurities in graphene, Phys. Rev. B **88**, 085441 (2013).

[44] V. I. Fal'ko, K. Kechedzhi, E. McCann, B. L. Altshuler, H. Suzuura, and T. Ando, Weak localization in graphene, Solid State Commun. **143**, 33 (2007).

[45] A. M. R. Baker, J. A. Alexander-Webber, T. Altebaeumer, T. J. B. M. Janseen, A. Tzalenchuk, L. Lara-Avila, S. Kubatkin, R. Yakimova, C.-T. Lin, L.-J. Li, and R. J. Nicholas, Weak localization scattering lengths in epitaxial and CVD graphene, Phys. Rev. B **86**, 235441 (2012).

[46] B. R. Matis, F. A. Bulat, A. L. Friedman, B. H. Houston, and J. W. Baldwin, Giant negative magnetoresistance and a transition from strong to weak localization in hydrogenated graphene, Phys. Rev. B **85**, 195437 (2012).

[47] J. Moser, H. Tao, S. Roche, F. Alzina, C. M. Sotomayor Torres, and A. Bachtold, Magnetotransport in disordered graphene exposed to ozone: From weak to strong localization, Phys. Rev. B **81**, 205445 (2010).

[48] E. McCann, K. Kechedzhi, V. I. Fal'ko, H. Suzuura, T. Ando, and B. L. Altshuler, Weak-Localization Magnetoresistance and Valley Symmetry in Graphene, Phys. Rev. Lett. **97**, 146805 (2006).

[49] X. Hong, S.-H. Cheng, C. Herding, and J. Zhu, Colossal negative magnetoresistance in dilute fluorinated graphene, Phys. Rev. B **83**, 085410 (2011).

[50] J.-L. Pichard, M. Sanquer, K. Slevin, and P. Debray, Broken Symmetries and Localization Lengths in Anderson Insulators: Theory and Experiment, Phys. Rev. Lett. **65**, 1812 (1990).

[51] N. M. R. Peres, F. Guinea, and A. H. Castro Neto, Coulomb interactions and ferromagnetism in pure and doped graphene, Phys. Rev. B **72**, 174406 (2005).

[52] E. H. Ahlgren, J. Kotaksoski, and A. V. Krasheninnikov, Atomistic simulations of the implantation of low-energy boron and nitrogen ions into graphene, Phys. Rev. B **83**, 115424 (2011).

[53] H. Miyazaki, K. Tsukagoshi, A. Kanda, M. Otani, and S. Okada, Influence of disorder on conductance in bilayer graphene under perpendicular electric field, Nano Lett. **10**, 3888 (2010).

[54] V. Ambegaokar, B. I. Halperin, and J. S. Langer, Hopping conductivity in disordered systems, Phys. Rev. B **4**, 2612 (1971).

[55] R. Lv, Q. Li, A. R. Botello-Mendez, T. Hayashi, B. Wang, A. Berkdemir, Q. Hao, A. L. Elias, R. Cruz-Silva, H. R. Guitierrez, Y. A. Kim, H. Muramatsu, J. Zhu, M. Endo, H. Terrones, J.-C. Charlier, M. Pan, and M. Terrones, Nitrogen-doped graphene: beyond single substitution and enhanced molecular sensing, Sci. Rep. **2**, 586 (2012).